Synchronous Compensators Considering Reactive Power for PLL Stability Improvement and Short-Circuit Ratio Evaluation

Jorge Suárez-Porras, *Student Member, IEEE*, Fidel Fernández-Bernal, Luis Rouco, *Senior Member, IEEE*, and Andrés Tomás-Martín

***Abstract*—This paper examines the impact of Synchronous Compensators (SC) on the stability of grid-following Inverter-Based Resources (IBRs), with a particular focus on the role of reactive power. Full-order simulation models of a commercial SC and a doubly-fed induction generator as the study model to represent the most complex IBR, are used. Using the short-circuit ratio (SCR) as the key index, the study confirms that the Phase-Locked Loop (PLL) in the IBR is crucial for system stability and shows that the reactive power injected by the SC plays a non-negligible role. It is shown that the main effect of the SC in the small-signal stability aspect is the Thévenin impedance seen by the PLL at the connection point, which, in the case of the SC, is the subtransient impedance and the SC reactive power. This idea is used to calculate the PLL eigenvalues movement easily. A new simple linear approximation model is proposed to estimate the correct SCR value for stability purposes considering the reactive power effect, as it is shown that the classical SCR measure does not fully capture the impact of the reactive power on the system stability.**

***Index Terms*—Synchronous compensator, short-circuit ratio, reactive power, IBR stability, PLL stability.**

NOMENCLATURE

A. Parameters and Variables

E_0''	SC subtransient internal voltage.
x_d''	SC direct-axis subtransient reactance.
Q_{SC}	SC supplied reactive power.
x_t	Transformer short-circuit reactance.
r_l	Transmission line resistance.
x_l	Transmission line reactance.
c_l	Transmission line capacitance.
K_Q	Slope in the linear relationship between SCR_{SC}^{st} and Q_{SC}.
K_{PLL}	Part of K_Q that is due to the effect of the PLL.
R^2	Coefficient of determination.
λ_{PLL}	Eigenvalue associated with PLL stability.
SCR_{NET}	SCR at the PCC considering only the grid line impedance.
$SCR_{NETlimit}$	Minimum SCR limit for network stability.
SCR_{PCC}	SCR at the PCC including grid line impedance and SC impedance.
SCR_{SC}	SCR contribution from the SC.
SCR^0	SCR_{SC} estimation with $Q_{SC}=0$.
$SCR_{SC}^{I_{CC}}$	SCR contribution from the SC based on its short-circuit current.
SCR^{PLL_red}	SCR for PLL stability based on a reduced model.
SCR_{SC}^{st}	Stability SCR contribution from SC.

B. Terms

CSCR	Composite Short-Circuit Ratio.
FOS	Full Order Simulations.
gSCR	Generalized Short-Circuit Ratio.
GSIM	Grid Strength Impedance Matrix.
HVDC-LCC	HVDC Line-Commutated Converter.
HVDC-VSC	HVDC Voltage-Source Converter.
IBR	Inverter-Based Resources.
MSG	Multipole Synchronous Generator.
MIPES	Multi-Infeed Power Electronic System.
PCC	Point of Common Coupling.
PLL	Phase-Locked Loop.
PV	Photovoltaic Generation.
RES	Renewable Energy Sources.
RMSE	Root Mean Square Error.
SC	Synchronous Compensator.
SCR	Short-Circuit Ratio.
SDSCR	Site-Dependent Short-Circuit Ratio.
VS	Voltage Stability.
WSCR	Weighted Short-Circuit Ratio.

Received 10 September 2024; revised 14 February 2025 and 23 May 2025; accepted 5 June 2025. Date of publication 9 June 2025; date of current version 23 February 2026. This work was supported in part by MICIU/AEI/10.13039/501100011033 under Project PID2021-125628OB-C21, in part by ERDF/EU under Grant PRE2022-101606, in part by ESF+, in part by MCIN/AEI/10.13039/501100011033 under Project TED2021-130610B-C22, and in part by European Union NextGenerationEU/PRTR. Article no. TEC-01011-2024. *(Corresponding author: Jorge Suárez-Porras.)*

The authors are with the IIT, ETSI ICAI, Universidad Pontificia Comillas, 28015 Madrid, Spain (e-mail: jsuarezp@comillas.edu).

Color versions of one or more figures in this article are available at https://doi.org/10.1109/TEC.2025.3578132.

Digital Object Identifier 10.1109/TEC.2025.3578132

I. INTRODUCTION

DECARBONIZATION is increasing the integration of renewable energy sources (RESs) into the power grid in the current global energy landscape. Synchronous generation is being replaced by RES worldwide to mitigate the dependence on fossil fuels.

The integration of RES is typically made through inverter-based resources (IBRs) at grid connection. IBR poses two main challenges in terms of inertia provision and stability, which is strongly related to short-circuit current and line impedances. Regarding inertia provision, the absence of a physical rotating mass in IBR systems makes it impossible to provide physical inertia to the connected system, although provision of virtual inertia from some kind of energy storage system is possible [1], [2]. Regarding short-circuit current, inverters are electronic devices constructed with semiconductors, which makes them weak to current overload. The conventional current limit for an inverter is approximately 1.1–1.2 times the rated current [3], [4]. This typically results in IBR systems with a very low short circuit ratio (SCR), which is a typical measure of system strength [3].

Synchronous compensators (SCs) have merged as a promising solution to tackle the challenges imposed by the high penetration of RES. SCs are synchronous generators that can not provide active power in steady-state but can deliver transient active power by extracting energy stored in the rotating mass, providing inertia to the system. In addition, synchronous compensator (SC) can enhance the system stability, providing reactive power compensation. Moreover, the SC is able to withstand an over-current 3-5 times its rated current [5], [6], making it an ideal choice for systems requiring an increased SCR. Note that, unlike conventional hydropower or thermal power plants, synchronous compensators do not provide active power control, as no prime mover supplies driving torque. This makes them different in their role in maintaining grid stability. This work focuses on SCs as facilitators for the integration of RES into the grid, particularly when there is a deficiency of SCR that the system operator defines as a requirement.

SCR provision from SC in power systems is well documented in previous studies [3], [4], [7], [8], [9], [10], [11], [12], [13]. It has been studied both from the small-signal [7] and from large-signal [9], [10] perturbation analysis points of view. This paper focuses on the stability of grid-following RES and the role of SCs in enhancing stability through the SCR contribution. Grid-following systems invariably include phase locked loop (PLL) mechanisms, which are crucial for their operation. This paper, in accordance with the previous literature, will confirm through detailed simulations in Section III that PLL plays a fundamental role in the stability of the system, and will assess the contribution of a commercial SC to the stability by the eigenvalue root-locus analysis using as reference index the SCR at the connection point. It will be shown that the effect of the SC is shifting the PLL root locus. In addition, the effect of the SC reactive power on the stability of the system is explored, showing that it is affected in a not negligible way.

Full-order simulations of large-scale electrical systems require significant effort and time. One of the devices that can be modeled with different levels of complexity is the SC. A fully SC detailed model is used in [3] to determine the optimal location of SC in weak grids to ensure short-circuit capability along the system. Similarly, a complete order model is also used in [4], [11], [12] for optimal location of SC in weak grids for SCR improvements and different purposes. However, when the SCR is the main focus of analysis, the SC can be modeled only with the subtransient impedance x''_d behind a voltage source E''_0 [13], as shown in Fig. 1.

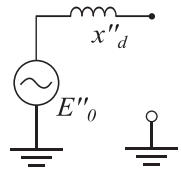

Fig. 1. Subtransient impedance model [13].

The subtransient impedance model is used in [8] where the optimal location of SC in weak grids is analyzed. In this paper, this simple subtransient impedance model is confirmed in Section IV to be a very good choice to estimate the new SCR, and a simple procedure is proposed to easily calculate the new PLL eigenvalues. However, when the SC reactive power is considered, this simple subtransient impedance model fails to capture the effect of the reactive power, both on the short-circuit current and stability. In addition, it is proved that the SCR, as a measure of the short-circuit current, does not capture the complete effect of the reactive power on the PLL stability. Therefore, in Section IV, two different simple linear models based on the subtransient impedance model are proposed to estimate the SCR when SC reactive power is considered. One for the SCR as a measure of the short-circuit current, and another one for the SCR as a reference index for stability.

The key contributions of this work are summarized as follows:

- It is shown that the reduced synchronous compensator (SC) model based on the subtransient impedance can accurately predict the position of the PLL eigenvalues of the DFIG, but only when the SC reactive power injection is zero.
- A linear model is proposed to calculate the SCR contribution of the SC in terms of short-circuit current, taking into account the SC reactive power injection operating point.
- A simplified simulation model is derived to validate the proposed linear model based only on the PLL dynamics of the system with the generators modeled as current sources.
- The proposed models allow for an accurate prediction of the eigenvalue locations of the IBR when an SC is connected, without requiring full-order simulation models.

The proposed model offers a simplified yet accurate method to estimate PLL stability, which is critical for the overall stability of the IBR-base power system, avoiding full-order simulations of the SC and maintaining sufficient accuracy for practical applications with reduced computational cost. For clarity, the full-order models of the doubly-fed induction generator (DFIG) and the SC, including their control systems, have been included in the appendices.

This paper is organized as follows. Section II discusses the definition of the SCR and presents several of its variations. In Section III, the small-signal stability of the system is analyzed as a function of the SCR for different reactive power operating points of the SC, using full-order simulations. Section IV focuses on the calculation of the SCR contribution from the SC from different perspectives and proposes a simplified model to estimate this contribution for stability analysis purposes. Section V

presents the main conclusions of the paper. Appendix A provides the parameters used in the DFIG model, and Appendix B includes the commercial SC model used in the simulations.

II. Short-Circuit Ratio Discussion

Short-circuit ratio (SCR) is a crucial concept in the study of power system stability. Currently, the value of the SCR is commonly accepted by system operators to determine the strength of a system [14], [15], [16]. The SCR can be viewed from two distinct perspectives. On one hand, the SCR can be seen as the physical response of a power system to a short-circuit fault. In case of a voltage dip at a point in the network, the SCR measures the ability to supply current at that point where the fault occurs so that the voltage profile of the network is altered as little as possible [17]. In an electrical system, where generators are connected to a point of common coupling (PCC), the SCR is defined as in [18], [19]:

$$SCR_{PCC} = \frac{S_{PCC}}{P_n} \tag{1}$$

where S_{PCC} is the network short-circuit power at the PCC prior to the RES connection in MVA, and P_n is the nominal active power of the RES in MW.

By choosing the nominal apparent power (S_n) of the RES as the base power of the per-unit (pu) system (the numerical value of $S_b = P_n$), and assuming that the voltage at the PCC is maintained at 1.0 pu, and that the DFIG is connected to the infinite grid through a single transmission line with impedance x_l the SCR in per-unit terms simplifies to [18]:

$$SCR_{PCC} = \frac{1}{x_l} \tag{2}$$

Then, SCR represents the equivalent admittance of the system in per-unit at the PCC. As will be shown in this study, the SCR plays a critical role in determining the stability of systems with grid-following IBRs.

On the other hand, the SCR can also be viewed from the perspective of system robustness and strength, through small-signal stability analysis [20], [21], [22], [23], [24], [25], [26]. In this context, the SCR is used to assess the stability margins of the system, which provide a measure of the system's ability to maintain stability in the face of small disturbances or perturbations. Analyzing the SCR from the small-signal perspective will identify potential weaknesses in the system and improve its stability. As will be shown in this paper, both perspectives (SCR as a measurement of short-circuit capability and the SCR as a measurement of stability) give different results for the SCR when the reactive power operating point is considered.

Modern electrical networks contain a significant amount of IBR penetration, and the controls of these IBR systems become relevant in the stability of the electrical system. The definition of SCR in (1) does not take into account the dynamics of the converter controls, which might cause an overestimation of the system's strength and stability. Variations of the SCR definition given in (1) arise to include the challenges imposed by the controls of electronic converters. The weighted short circuit ratio (WSCR) weights the SCR by the size of each IBR connected to the PCC [22]. The composite short circuit ratio (CSCR) takes into consideration the nominal power of the IBR and the short circuit power provided by the rest of the elements [18], [23]. The site-dependent short circuit ratio (SDSCR), proposed by [24], takes into consideration the SCR dynamics interaction among items connected to the grid. Finally, a concept proposed in [25] is the so-called generalized short-circuit ratio (gSCR), which quantifies the power grid strength in a multi-infeed power electronic system (MIPES). Among all definitions, the common factor lies in the SCR reduction when IBRs generation increases in a system. While the SCR is widely used as an indicator of system strength, alternative methods have been proposed to analyze the stability of power electronic systems more comprehensively. Notably, the concept of voltage stiffness (VS) introduced by [27], and the grid strength impedance matrix (GSIM) proposed by [28] offer dynamic perspectives that account for the control interactions within inverter-based resources. However, the classical SCR is the parameter that network operators use to allow access to the grid for new installations [14], [15], [16]. In fact, given an SCR for which the system is stable, if the SCR increases, the stability increases, and vice-versa [26]. For this reason, classical SCR is widely used and it is the one used in this paper.

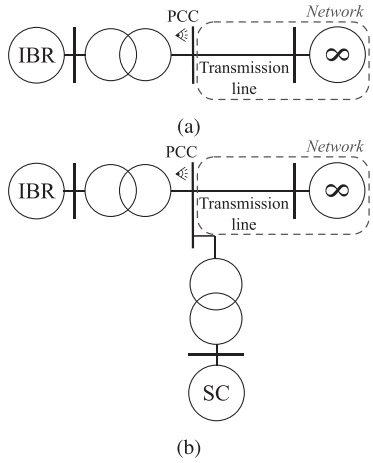

Fig. 2. One-line diagram of the system under study. (a) base case of an IBR connected to the network through a transmission line and (b) the SC is connected to the PCC.

III. Full-Order Stability Analysis Including SC Reactive Power Operating Point

A. System Description and Procedure

First, as shown in Fig. 2(a), the IBR is connected to an ideal network through a transmission line and the line length is increased to find the stability limit of the IBR connected to the PCC. Then, the SCR *seen* by the IBR at the PCC, SCR_{PCC}, is calculated. In this first case, it is the contribution of the network through the transmission line at the PCC. If the line resistance is neglected (3) [18], [19], [29]:

$$SCR_{PCC} = SCR_{NET} \approx \frac{1}{x_l(pu)} \tag{3}$$

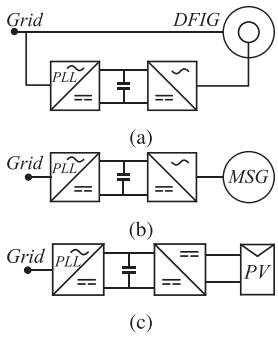

Fig. 3. Simplified models of grid-following inverter-based resources renewable energy sources. (a) DFIG model, (b) MSG model and (c) PV model.

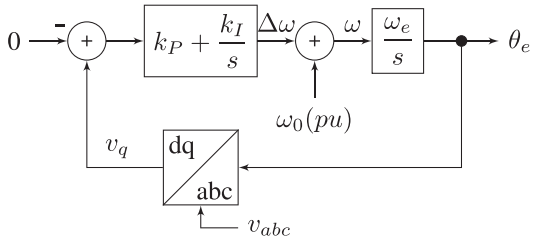

Fig. 4. Phase locked loop block diagram.

where x_l is the line reactance in the per unit system of the power system. The SCR_{NET} will be used as the reference index for the stability analysis. Then, as shown in Fig. 2(b), the SC is connected to the system at the PCC to analyze how stability is improved.

RES can be of various types. Typically, RES are connected to the grid through IBRs. Fig. 3 shows three simplified illustrations of renewable generation models: a DFIG, a multipole synchronous generator (MSG) and a photovoltaic (PV) module. If the converter connected to the grid side is a grid-following converter, the current control is made with respect to the grid voltage, and therefore there is a PLL. The typical structure of the PLL is shown in Fig. 4.

In addition, in all of them, there is a DC side and an AC side. In Fig. 3(b), the dynamics of the two AC sides are decoupled from each other due to the DC-link bus. In Fig. 3(c), the dynamics from the PV side are decoupled from the AC side through the DC-link bus. This decoupling does not occur in the DFIG, where the dynamics of both converters influence each other through the stator-rotor of the induction machine. Given this additional interaction between the converters on both sides of the DC-link bus, it has been decided to use the DFIG as the study model to represent the most complex RES.

The DFIG is connected through an equivalent transformer sum of the low-to-medium-voltage transformer and the medium-to-high-voltage transformer. Values of 6% and 9% will be taken for their short-circuit impedances, respectively. The DFIG model is taken from [30]. The doubly-fed induction machine is implemented with a full-order model. Four controllers are implemented, taken from [31]: The grid-side converter is responsible for maintaining the DC-link bus voltage and for keeping the reactive power commanded to 0 to reduce the converter loading [32], [33]. The rotor side converter controls the optimum electromagnetic torque by a q-axis current control-loop and the stator reactive power by a d-axis current control-loop, set to 0 so that the DFIG only injects active power to the grid. The DFIG is generating nominal power, i.e., $P_{DFIG} = 1$ pu. DFIG model and controllers are described in Appendix A.

The SC is placed at the PCC through a 10% impedance transformer. The SC full machine model and the transmission lines are taken from [13]. The SC model values come from a commercial SC, which can be found in Appendix B.

The π-model has been adopted for the transmission line, having a reactance (x_l) of 0.001 pu/km, a resistance (r_l) of 10% the line reactance, and a susceptance (c_l) of 0.0005 pu/km at each terminal.

The system begins with a short line ($L = 50$ km), and the line length is increased, i.e., the SCR is reduced. As the system's topology is changed at every iteration, modal analysis computation and the power flow are computed at every line distance change. Eigenvalues are computed at each line length to verify the system's stability.

B. Base Case: Analysis Without SC

There is a variety of research on small-signal stability analysis of IBR without SC and the relationship with the SCR [26], [34], [35], [36]. In all of them, the PLL control-loop gains are modified to obtain the eigenvalues location for several specific SCRs. In [26], a multi-infeed power electronic system (MIPES) with several converters connected to the grid is analyzed. It is concluded that the PLL control-loop can cause instability issues in the system when the short circuit ratio is decreased. In [34], a high-voltage direct current - line commutated converter (HVDC-LCC) system is studied, concluding that the PLL can cause instability issues under weak-grid scenarios. A similar conclusion can be found in [35] where a high-voltage direct current - voltage source converter (HVDC-VSC) is taken as the system under study. In [36], a DFIG system is analyzed for two SCR cases, obtaining a similar conclusion, although there is no clear assignation of the eigenvalues obtained and the subsystems associated with them.

As mentioned earlier, a different approach is adopted in this paper: the PLL control-loop gain is kept constant and the line length is increased (the SCR is decreased).

The model considered as the base case in this paper is the connection between the grid and the DFIG through a transmission line with no SC installed. The line impedance is increased from 50 km ($SCR_{NET} = 20$) to 200 km ($SCR_{NET} = 5$). Results are shown in Fig. 5.

The minimum SCR that the DFIG can withstand under the specified control configuration is $SCR_{NETlimit} = 10.3$ (red triangles in Fig. 5):

$$SCR_{NETlimit} = \frac{1}{x_l} = \frac{1}{97.5 \text{ km} \cdot 0.001 \text{ pu/km}} = 10.3 \quad (4)$$

It is worth noting that the minimum SCR could potentially be further reduced through appropriate tuning of the DFIG control

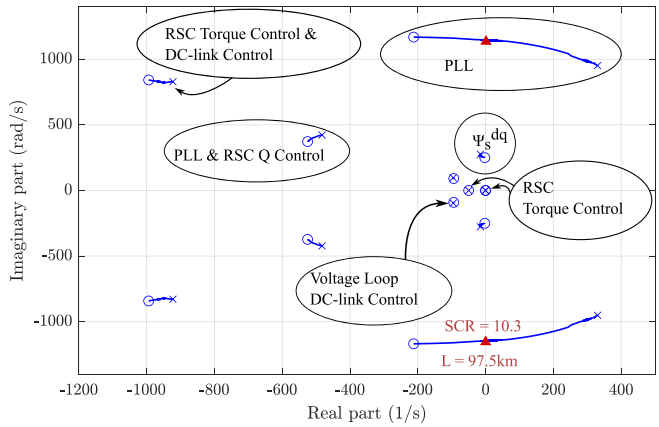

Fig. 5. Root-locus for the base case without SC when the SCR is varied from 20 (crosses, 50 km) to 5 (circles, 200 km).

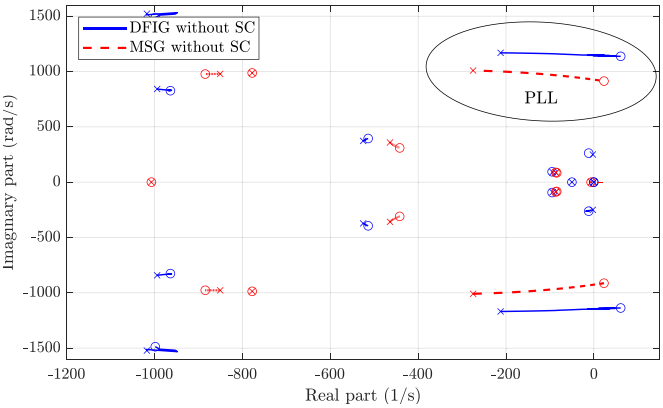

Fig. 6. Comparison of DFIG and MSG stability as the transmission line length increases from 50 km (SCR = 20) to 105 km (SCR = 9.5) demonstrating the PLL is the casue of the system instability.

loops. However, in this work, the focus remains on evaluating the role of the synchronous compensator in supporting the DFIG at a specific operating point without altering the existing control parameters.

By computing the system's participation factors using the definition in [37], the eigenvalues can be associated with the different DFIG subsystems, as shown in Fig. 5. In accordance with the literature, the eigenvalues that make the system unstable are the ones associated with the PLL subsystem [26], [34], [35], [36]. This is a very important fact because the PLL, as shown in Fig. 3, is common to all RES in which a PLL control-loop is needed.

To further support the generalization of the proposed method to other RES, Fig. 6 compares the stability behavior of the DFIG and an MSG system. Both systems use a PLL, and the simulation demonstrates that the PLL is the primary source of instability as the transmission line length increases. Since the MSG is based on a full-converter topology, it is expected that this behavior can also extend to other full-converter-based systems, such as PV systems. While the results suggest that the proposed method can generalize to other RES, a more detailed validation for specific models exceeds the scope of this work.

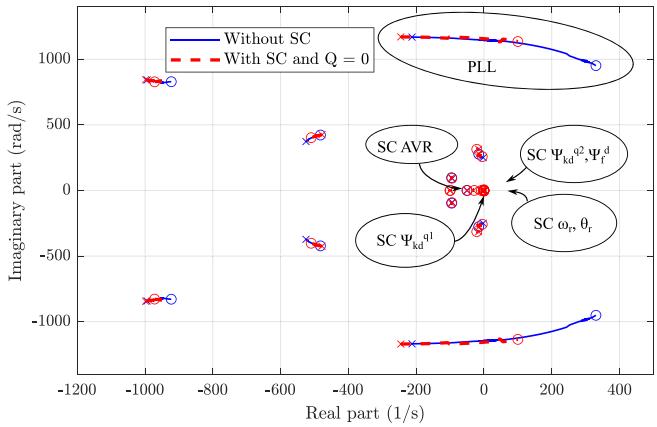

Fig. 7. Root-locus for the base case without SC and with SC injecting no reactive power when the SCR is varied from 20 (crosses, 50 km) to 5 (circles, 200 km).

C. Analysis With SC Producing No Reactive Power

The same process is carried out but with the SC connected at the PCC first injecting no reactive power using a SC full-order model (see Appendix B). Fig. 7 shows the system's root-locus when the SCR_{NET} is varied from 20 (crosses, 50 km) to 5 (circles, 200 km) when the SC is connected to the system. Note that although the SC contributes to the SCR at the PCC:

$$SCR_{PCC} = SCR_{NET} + SCR_{SC} \tag{5}$$

the SCR at the PCC is calculated as in (2) because it is intended to use the impedance line value as a reference index for both cases, with no SC and with SC.

As shown in Fig. 7, the location of the PLL eigenvalues moves to the left side of the stability plane, making the system much more stable. In fact, the value of the SCR_{NET} for stability increases from 10.3 to 14.3. Note that the new root-locus is almost the same as the base case without SC but shifted to the left (i.e., to the more stable region). This fact will be used in Section IV-B to propose a simple method based on the SC SCR contribution to estimate the new PLL eigenvalues from the original root-locus without SC when an SC is connected to the system.

D. Impact of SC on Stability and the SCR Considering SC Reactive Power Operating Point

The same process is carried out, but now with the SC injecting or absorbing certain amount of reactive power. Fig. 8 shows the root-locus for three reactive power injections of the SC. It can be seen in Fig. 8 that the complex pair of eigenvalues related to the DFIG PLL are affected by the SC reactive power injection. It can be observed that, for the operating points in which the SC injects reactive power, $Q_{sc} > 0$, the eigenvalues associated with the PLL are more damped and better stability limits are obtained. And the opposite when $Q_{sc} < 0$. In fact, the $SCR_{NET} = 14.25$ when $Q_{sc} = 0$, reduces to $SCR_{NET} = 12.95$ for $Q_{sc} = -0.5$ pu, and increases to $SCR_{NET} = 15.95$ when $Q_{sc} = 1$ pu. This will be shown in terms of the SC SCR

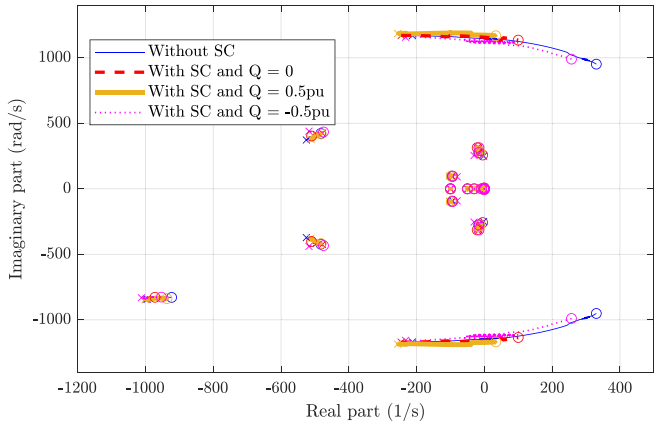

Fig. 8. Root-locus in a DFIG without and with the SC with different reactive power operating point conditions when the SCR is varied from 20 (crosses, 50 km) to 5 (circles, 200 km).

contribution in Section IV. Note that even with $Q_{sc} = -0.5$ pu in Fig. 8, the PLL eigenvalues are more stable than without the SC.

The root-locus when $Q_{sc} \neq 0$, although not identical, is very similar to the base case with no SC but shifted more or less to the left (depending on the reactive power). For this reason, the same method to estimate the new PLL eigenvalues proposed in Section IV-B for the case with $Q_{sc} = 0$ is still applicable to the case in which $Q_{sc} \neq 0$ in Section IV-C.

IV. Estimation of the SC SCR Contribution Considering SC Reactive Power

The SC SCR contribution to the system from the stability point of view, SCR^{st}_{SC}, is calculated from the detailed simulations as the difference between the SCR with the SC installed ($SCR_{NETfinal}$) and the SCR when the SC is not installed (SCR_{NETini}):

$$SCR^{st}_{SC} = SCR_{NETfinal} - SCR_{NETini} \tag{6}$$

This method of calculating the SC SCR contribution to the system will allow comparing the results from the detailed simulations with the results obtained using the classical SC SCR contribution based on the short-circuit current, SCR^{0}_{SC}. As will be shown, SCR^{0}_{SC}, will differ from the SCR^{st}_{SC} when reactive power injection is considered. A flowchart is shown in Fig. 9 explaining the procedure to calculate the SCR when the system becomes unstable when the SC is installed.

A case study is selected based on Fig. 5. Starting from the base case without SC where the DFIG becomes unstable, i.e., $SCR_{NETini} = 10.3$ ($L = 97.5$ km), the aim is to determine $SCR_{NETfinal}$ when the commercial SC described in the Appendix B is installed.

A. Classical SCR_{SC} Estimation With $Q_{SC} = 0$: SCR^{0}_{SC}

The current response in a short-circuit at a SC terminals can be classified into three stages: the subtransient, transient, and steady-state stages. In the subtransient stage, the stator flux linkages are assumed to be constant. Only the damping circuits' effect is considered in this stage, as they impact the subtransient current response the most [13].

Typically, when the SCR is the main concern in the simulation study, the SC model is reduced to the d-axis subtransient

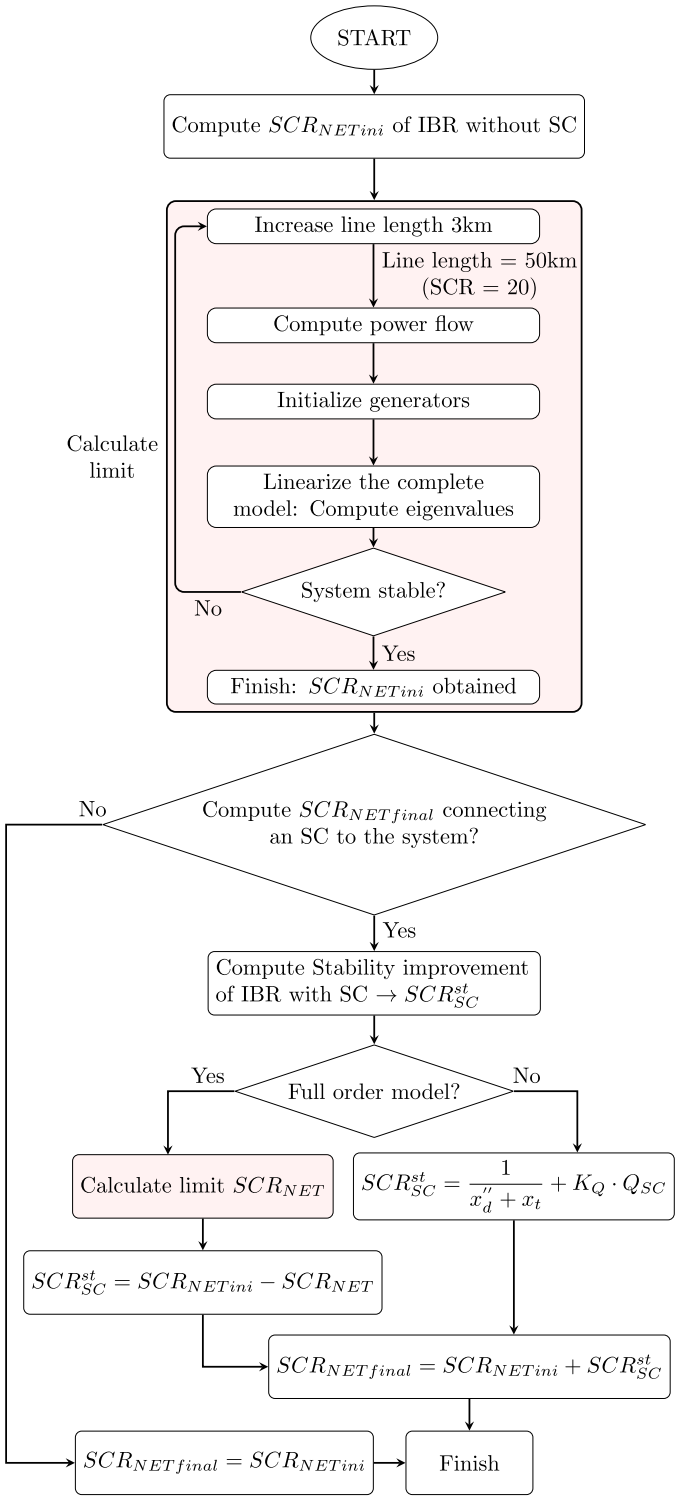

Fig. 9. Flowchart illustrating the SCR stability evaluation process for IBR systems with and without SC.

TABLE I
LOOK-UP TABLE OF EIGENVALUES FOR FIGS. 10 AND 11

Row	Line (km)	SCR	λ_1	λ_2	$\cdots$	λ_n
1	50	20	λ_{11}	λ_{12}	$\cdots$	λ_{1n}
⋮	⋮	⋮	⋮	⋮	⋮	⋮
b †	70	14.3	λ_{b1}	λ_{b2}	$\cdots$	λ_{bn}
⋮	⋮	⋮	⋮	⋮	⋮	⋮
a †	97	10.3	λ_{a1}	λ_{a2}	$\cdots$	λ_{an}
⋮	⋮	⋮	⋮	⋮	⋱	⋮
m	200	5	λ_{m1}	λ_{m2}	…	λ_{mn}

† Dark blue represents the root-locus without SC, and light red represents root-locus estimation when the SC is installed.

impedance, as in Fig. 1, neglecting the effect of the stator resistance. Therefore, the SCR contribution of a SC is usually expressed only with the d-axis subtransient impedance x''_d, and taking $E''_0 = 1$ [8], [13], [38]:

$$SCR^{Icc}_{SC}\Big|_{Q_{SC}=0} = SCR^{0}_{SC} = \frac{E''_0}{x''_d}\Big|_{E''_0=1} = \frac{1}{x''_d} \tag{7}$$

As the SC is connected to the PCC through a transformer, (7) is rewritten as:

$$SCR^{Icc}_{SC}\Big|_{Q_{SC}=0} = SCR^{0}_{SC} = \frac{1}{x''_d + x_t} \tag{8}$$

In the case study developed in Section III-D, starting from an $SCR_{NETini} = 10.3$, by substituting the value of the subtransient impedance and the transformer impedance from Appendix B into (8), it is found that the SCR contribution from the SC at the PCC using the subtransient model (SCR^0_{SC}) is:

$$SCR^{0}_{SC} = \frac{1}{x''_d + x_t} = \frac{1}{0.15 + 0.1} = 4 \tag{9}$$

From Section III-D, with the SC full-order model and $Q_{SC} = 0$, the $SCR_{NETfinal} = 14.25$ and therefore $SCR^{st}_{SC} = SCR_{NETfinal} - SCR_{NETini} = 14.25 - 10.3 = 3.95$.

Comparing the value obtained with the full-order model, 3.95, with the value calculated using (9), the error is just 1%. This indicates that SCR^0_{SC} is a very accurate estimator of SCR^{st}_{SC} when $Q_{SC} = 0$.

B. PLL Root-Locus Estimation Using SCR^0_{SC}

If the IBR root-locus for the base case without the SC is known in terms of the SCR_{NET} (by increasing the line length, as in Fig. 5), the SCR^0_{SC} value given by (8) can be used to estimate the location of the new eigenvalues in case of installing an SC next to the IBR neglecting the effect of the SC reactive power on the SCR. This can be accomplished without the need to repeat simulations, including the full-order SC model. If the IBR root-locus without the SC is in a look-up table form, as in Table I, the new root-locus estimation when an SC is installed, is carried out by shifting between rows in the table due to the fact that the root-locus with SC is the same as the base case without SC

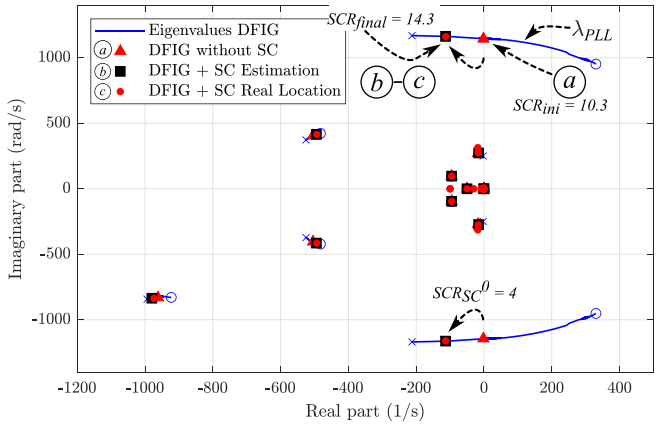

Fig. 10. Root-locus for the case without SC when the SCR is varied from 20 (crosses, 50 km) to 5 (circles, 200 km).

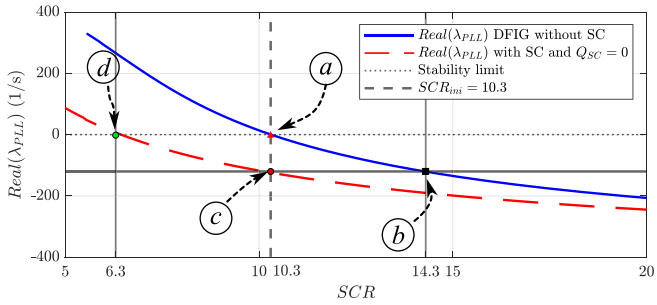

Fig. 11. Real part of the eigenvalue mostly related to the PLL-control-loop for the base case without SC and with SC producing no reactive power when the SCR is varied from 20 (50 km) to 5 (200 km).

but shifted to the left to the more stable region (see Fig. 7). It should be noted that, by introducing the SC into the system, the SCR_{PCC} seen from the DFIG is increased, meaning that the impedance seen from the DFIG is reduced.

As an example, let us consider from the base case (with no SC), the point in which the DFIG becomes unstable: row a in Table I, $SCR_{PCCini} = SCR_{NETini} = 10.3$, point ⓐ in Fig. 10 (Fig. 5 is reproduced in Fig. 10 for ease of explanation). By (9) the new DFIG eigenvalue location can be accurately estimated just by calculating the new $SCR_{PCCfinal} = SCR_{PCCini} + SCR^0_{SC} = 10.3 + 4 = 14.3$, and then looking up in the table the new SCR (row b in Table I, $SCR = 14.3$, point ⓑ in Fig. 10).

As the eigenvalue yielding to unstable operation is mostly related to the PLL control-loop (λ_{PLL}), Fig. 11 shows the real part of the eigenvalue λ_{PLL} in terms of the SCR. When the SC is not installed, the SCR limit value can be obtained when $Real(\lambda_{PLL}) = 0$ (point ⓐ in Fig. 11). If the commercial SC is installed, $SCR = 14.3$, and the new λ_{PLL} eigenvalue can be obtained just by looking for the new $SCR = 14.3$ in the curve with no SC, point ⓑ in Fig. 11. There is no need to calculate a new curve from a detailed simulation with the SC installed. Note that point ⓑ is more stable than point ⓐ because $Real(\lambda_{PLL}) < 0$.

To validate this fact, the results for the full-order model simulation with the commercial SC are shown in the dashed line

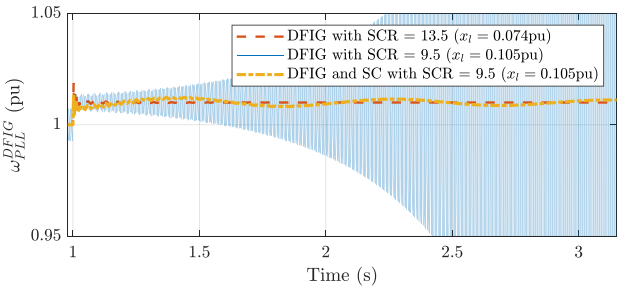

Fig. 12. Output frequency of the DFIG's PLL under different SCR with and without SC with $Q_{SC} = 0$.

in Fig. 11. Note that the value of the SCR that has to be used now in Fig. 11 has to be the $SCR_{NETini} = 10.3$ and not the $SCR_{PCCfinal} = 14.3$ because simulation results are tabulated for the SCR_{NET}. That is to say, the SCR in Fig. 11 is the one associated with the line impedance (line length) to which the SC is to be connected. It can be seen that at $SCR = 10.3$, point ⓒ has the same real part as point ⓑ, meaning that, as can be seen in Fig. 10, corresponds to the same PLL eigenvalues. In addition, and as expected, the system can operate in the stable region for greater line lengths (point ⓓ, $SCR_{NET} = 6.3$), when the SC is installed next to the IBR.

Time-domain simulations have also been performed to show the contribution of the SC to the stability of the system in the time domain. These simulations apply a 1% step change at $t = 1$ s in the infinite grid output frequency to which the DFIG (and SC) are connected. The results of two experiments are presented in Fig. 12:

- First experiment: The DFIG is simulated without the SC under two conditions:
  - When the SCR is high ($SCR = 13.5$, line impedance = 0.074 pu), demonstrating that the DFIG remains stable.
  - When the SCR is low ($SCR = 9.5$, line impedance = 0.105 pu, being the stability limit 10.3, as described in (4)), demonstrating that the DFIG becomes unstable.
- Second experiment: The DFIG is simulated with the SC providing $Q_{SC} = 0$. With a $SCR = 9.5$ (line impedance of 0.105 pu), the DFIG becomes stable due to the contribution of the SC.

These time-domain results visually confirm the stabilizing effect of the SC under weak grid conditions, even with no reactive power injection.

An important conclusion derived from the analysis in Fig. 11, is that the effect of installing an SC is to reduce the apparent length line and the apparent line impedance that is seen by the PLL control-loop. In this example, from an actual line length of 97.5 km ($SCR_{NETini} = 10.3$), $x_l = 1/10.3 = 0.097$ pu to 70.2 km ($SCR_{NETfinal} = 14.3$), $x_l = 1/14.3 = 0.07$ pu. This change in the impedance value seen by the PLL control-loop is easily explained in terms of SCR_{PCC} when the SCR is seen as the equivalent admittance of the system at the PCC as shown in (2): the new impedance is just the parallel of the line impedance, x_l, and $(x''_d + x_t)$.

Fig. 13 shows the proposed equivalent circuit representing the Thévenin impedance seen from the IBR to easily calculate

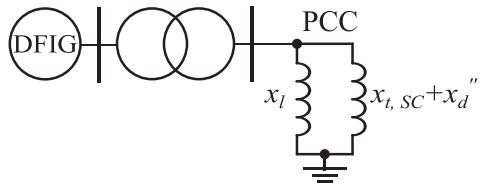

Fig. 13. Equivalent circuit representing the Thévenin impedance seen from the IBR model.

the impedance seen from the PLL control-loop, accounting for the line impedance and the SC subtransient and transformer impedances when no SC reactive power is considered.

This figure explains why the root-locus of the system with no SC is so similar to the system with SC: from the point of view of the PLL, there is no such a SC connected to the PCC but just a change in the impedance value. This technique and this conclusion could be easily generalized and applied to any generator/device, not only to a SC. For instance, a STATCOM may also be modeled as a Thévenin in a small-signal linearization process. In addition, as will be shown in Section IV-C, an additional virtual impedance will be included in the circuit model to account for the SC reactive power operating point.

C. Estimation of the SCR_{SC} Including Q_{SC}

As it has been shown in Section III-D, SC reactive power injection, Q_{SC}, affects system stability and the SCR_{SC}^{st} value. However, SCR_{SC}^{0} does not consider Q_{SC}. If the reactive power operating point of the SC is taken into account with the SC full order model, SCR_{SC}^{st} ranges from 2.98 to 6.05, when Q_{SC} ranges from -0.5 pu to 1 pu, and SCR_{SC}^{0} does not account for this change (see the second and fifth columns of Table II). Although from the conclusions drawn in the last part of Section IV-B, the Thévenin impedance seen by the PLL is a key factor in the stability of the system, it is not the only one that affects stability. Clearly, the reactive power in the PCC plays a role. This is explained by the fact that the PLL tries to track the voltage space vector at the terminals of the IBR, and voltage quality and voltage stability closely depend on reactive power.

SCR_{SC}^{0} estimation given by (7) can be improved considering the effect of Q_{SC} on the value of E_0'' (instead of considering $E_0'' = 1$ as it is done in (7)). For a given Q_{SC}, and because the SC does not produce steady-state active power, $i_d^{SC} = Q_{SC}$ and $i_q^{SC} = 0$ in the dq SC reference frame, assuming $v_{PCC} = v_{d,PCC} + jv_{q,PCC} = 0 + j1$ pu due to the dq-axis voltage alignment. E_0'' is the pre-disturbance value of the internal voltage given by [13]:

$$E_0''\Big|_{t=0^-} = |v_{PCC} + jx_d'' \cdot i_d^{SC}| = 1 + x_d'' \cdot Q_{SC} \tag{10}$$

Then, SCR_{SC} can be estimated by:

$$SCR_{SC}^{Icc} = \frac{E_0''}{x_d''} = \frac{1}{x_d''} + Q_{sc} \tag{11}$$

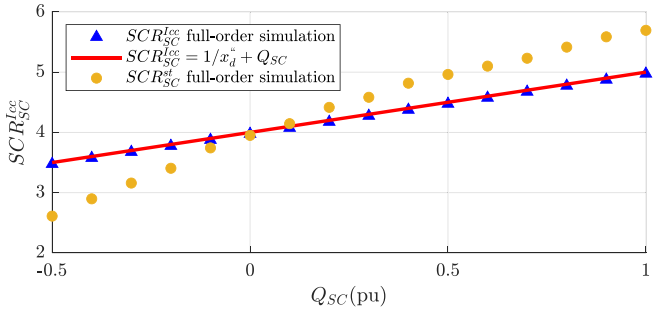

Fig. 14. First instants SC short-circuit current contribution at different SC reactive power operating points. Results for SCR^{st}_{SC} is shown for comparison.

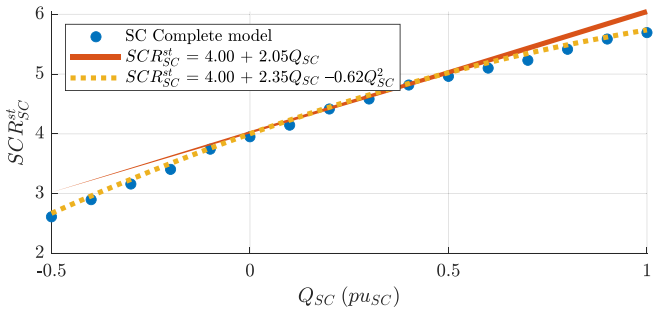

Fig. 15. SCR contribution of a full-order model reactive power injection is varied from -0.5 pu to 1 pu with a linear and a quadratic approximation.

and including the transformer impedance between the SC and PCC,

$$SCR^{Icc}_{SC} = \frac{1}{x''_d + x_t} + Q_{sc} = SCR^0_{SC} + Q_{sc} \tag{12}$$

Equation (12) indicates that the SCR should increase or decrease approximately linearly (approximately because (12) is derived from a simplified model), with the value of Q_{SC} with a slope of 1.

Full-order simulations removing the DC transient for the commercial SC of Appendix B have been carried out to obtain the exact SCR^{Icc}_{SC} value when a short-circuit occurs at the SC terminals (after the SC transformer impedance ($x_t = 0.1$ pu)), making $SCR^{Icc}_{SC} = |\vec{I}|$ (modulus of the stator space vector current) in the first instants. It can be seen in Fig. 14 that real short-circuit current contribution from the SC can be accurately captured by (12). In addition, Fig. 14 includes the full-order simulation results for SCR^{st}_{SC} using the commercial SC described in Appendix B. As can be observed, the SCR^{st}_{SC} varies approximately linearly with Q_{SC} according to the mathematical deduction given in (12), but with a different slope: 2.05 instead of 1 (see Fig. 15). This means that, although short-circuit current including reactive power correction, i.e. SCR^{Icc}_{SC}, is very well estimated by (12), it fails to include the whole effect of the Q_{SC} on the PLL stability (see the third and fifth columns of Table II).

Different polynomial interpolations of varying orders have been analyzed using the full-order simulation results. Among them, a quadratic interpolation of the form given in (13) shows an excellent fit, with a coefficient of determination of $R^2 = 0.99$

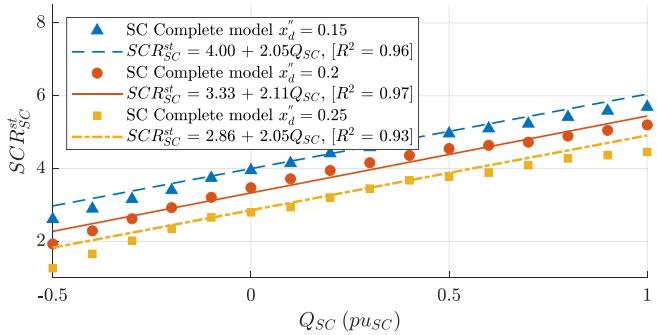

Fig. 16. SCR contribution of a full-order model with 3 different x''_d values and reactive power injection is varied from -0.5 pu to 1 pu.

and a root mean square error (RMSE) of 0.067.

$$SCR^{st}_{SC} = SCR^0_{SC} + K_{Q1} \cdot Q_{SC} + K_{Q2} \cdot Q^2_{SC} \tag{13}$$

These results suggest that the functional relationship between SCR^{st}_{SC} and Q_{SC} is likely to follow a quadratic form. This functional structure is further supported by the simulation results shown later, using a simplified simulation model with a generic IBR.

In addition, a linear interpolation also provides a strong fit, with a coefficient of determination of $R^2 = 0.96$ and a root mean square error (RMSE) of 0.195. Both interpolation results, along with the full-order simulation reference, are depicted in Fig. 15.

Taking the linear approximation as a practical and sufficiently accurate approximation of the full-order model as suggested by the former results, (12) is modified to:

$$\left[\begin{cases} SCR^{st}_{SC} = SCR^0_{SC} + K_Q \cdot Q_{SC}, \\ K_Q = 1 + K_{PLL} \end{cases}\right] \tag{14}$$

where SCR^0_{SC} is given by (8), and K_Q would mainly depend on the PLL parameters, with $K_Q = 2.05$ the value obtained from a linear interpolation of the full-order simulation results for the specific typical parameters used in this paper. Note that K_Q includes the effect of the increase in the short-circuit current provided by the SC due to the Q_{SC} (slope 1 in (12)), and an additional (virtual) short-circuit current due to the interaction of the Q_{SC} with the PLL (K_{PLL}), that in this specific case is as much as $K_{PLL} = 1.05$ (as will be later demonstrated with the simulation model provided in Fig. 19).

Different experiments have been carried out to validate the generality of the linear approximation of SCR^{st}_{SC} given by (14). First, the subtransient impedance x''_d has been modified for three cases: $x''_d = 0.15$ (base case), $x''_d = 0.2$ and $x''_d = 0.25$, as usual values of x''_d range between 0.15 pu and 0.3 pu [13]. The simulation results are shown in Fig. 16. Linear approximations using (14) and R^2 values for different x''_d can be found in Fig. 16 legend.

From the linear approximations in Fig. 16, it can be calculated that, by increasing $\Delta x''_d = 33.3\%$ and 66.6%, $\Delta K_Q = -2.38\%$ and -5.91%, respectively. Therefore, it is verified that the slope is little affected by x''_d. To further validate the accuracy of (14) in predicting the SCR contribution of the synchronous compensator, additional simulations were conducted to analyze

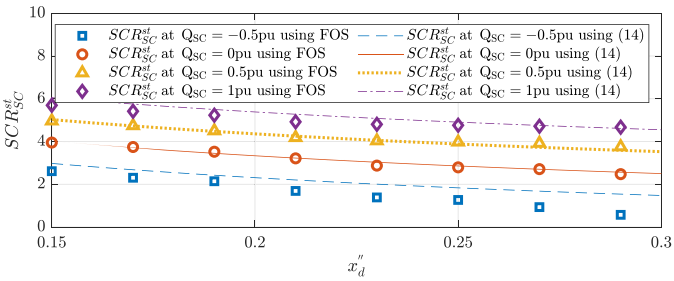

Fig. 17. Comparison of the Full-Order Simulation (FOS) versus (14) for obtaining SCR^{st}_{SC} for different values of Q_{SC} with x''_d varying from 0.15 pu to 0.3 pu.

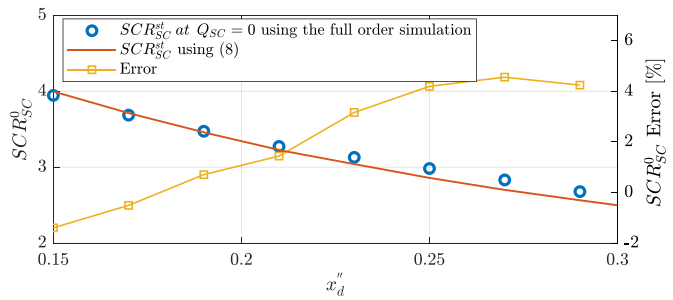

Fig. 18. Full-order model SCR^{st}_{SC} simulation with $Q_{SC} = 0$, SCR^{0}_{SC} using (8) and relative error with x''_d varying from 0.15 pu to 0.3 pu.

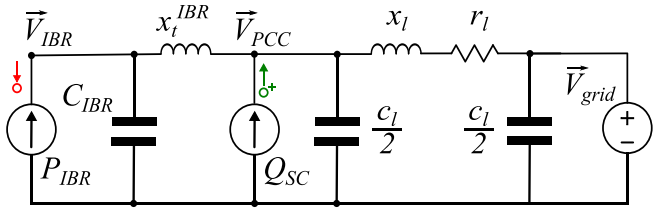

Fig. 19. One-phase diagram of the simplified model used for the simulation analysis of the PLL stability. Generators are configured as current-sourced to generalize the results to any IBR.

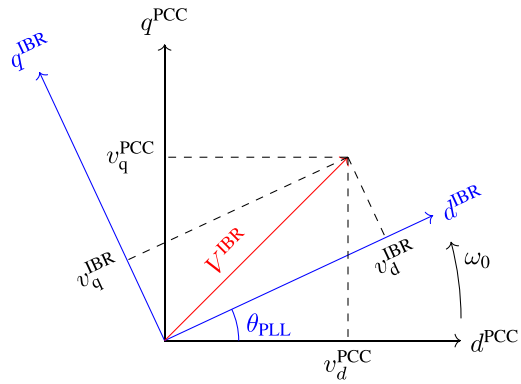

Fig. 20. Angle transformation from the angle at the PCC to the angle measured in the IBR capacitor (V_c^{IBR}).

the impact of x''_d on the SCR for different values of Q_{SC}. The results of these simulations are presented in Fig. 17. As shown in Fig. 17, the SCR values obtained using (14) closely match those obtained through Full-Order Simulations (FOS). This consistency demonstrates the capability of (14) to provide reliable predictions of the SC's impact on system stability without the need to carry out complex full-order simulations.

In addition, as x''_d is relevant for computing SCR^0_{SC}, several simulations have been carried out to analyze the effect of x''_d on the accuracy of the estimation of SCR^0_{SC}. Results are shown in Fig. 18. As can be seen, estimating SCR^0_{SC} using (8) yields to an error below 5%. The absolute error is 4.2% when $x''_d = 0.29$ and -1.4% when $x''_d = 0.15$.

To check that the former results may apply to other RES different from a DFIG, a simplified simulation model with a generic IBR has been developed to analyze the PLL stability while maintaining the essential dynamics of the system. This model accounts for the dynamics of inductances, capacitors, and the PLL, while the generating units are represented as current sources with first-order dynamics responses. The simplified system model is shown in Fig. 19.

The system consists of a generic IBR connected to the PCC through a transformer with an impedance x_t^{IBR} that has been set to j0.15 pu. The PCC is connected to an infinite bus via a transmission line with impedance $z_l = r_l + jx_l$, where $r_l = 0.1 \cdot x_l$. A current source, representing the reactive power injection from the SC into the PCC with a first-order approximation to represent the sub-transient time constant, that has been set to 30 ms (see Table IV), with Q_{SC} varying from -0.5 pu to 1.0 pu. The IBR injects active power $P_{IBR} = 1$ pu and no reactive power ($Q_{IBR} = 0$) with a first-order time constant to reflect the dynamics from the torque control-loop, as reflected by τ_{wr} in the low-pass filter in the torque control-loop in Fig. 25 (see Table III). This time constant has been set to a 100 ms. The IBR voltage space-vector, $\vec{V}^{IBR}$, can be computed by solving the system in Fig. 19.

The PLL measures the voltage $\vec{V}^{IBR}$ and adjusts its angle θ_{PLL} to align the d-axis with this voltage ($v_q^{IBR} = 0$). The angle computed by the PLL control with respect to the angle at the PCC is graphically shown in Fig. 20, being ω_0 the system base frequency. It should be noted that the space-vector $\vec{V}^{IBR}$ would be aligned in steady-state with the d-axis of the IBR imposed by the PLL (d^{IBR}) so that $v_q^{IBR} = V^{IBR}\sin(\theta_{PLL})$.

The dynamics of the PLL are given by:

$$\dot{\theta}_{PLL} = \omega_{PLL} = \omega_{\text{ref}} + K_p v_q^{IBR} + K_i \int v_q^{IBR}\, dt. \qquad (15)$$

and substituting v_q^{IBR}:

$$\dot{\theta}_{PLL} = \omega_{PLL} = \omega_{ref} + K_p \left(V^{IBR}\sin(\theta_{PLL})\right) + K_i \int \left(V^{IBR}\sin(\theta_{PLL})\right) dt. \qquad (16)$$

For each operational point of the SC, characterized by different values of Q_{SC}, the maximum transmission line length beyond which the system becomes unstable is analyzed. This analysis is carried out using numerical methods. The procedure involves determining the transfer function of the system, where the input is Q_{SC} and the output is the IBR voltage measured by the PLL, $\vec{V}^{IBR}$. By analyzing the system eigenvalues as the line length increases, the critical SCR ($SCR_{critical}$) is identified for each

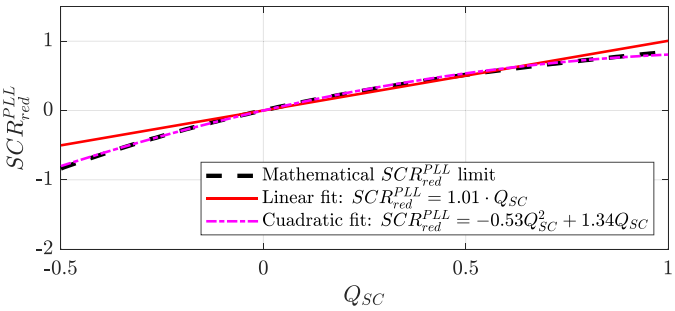

Fig. 21. SCR limit due to PLL unstability from the simulation results of the reduced system of Fig. 19. Linear and cuadratic approximations are fitted to the obtained data.

Q_{SC} value. Then, by considering the critical SCR when there is no contribution from the SC ($SCR_{critical}^{Q_{SC}=0}$), i.e. when $Q_{SC} = 0$, the SCR of the reduced system for the PLL stability analysis (SCR_{red}^{PLL}) can be computed as in (17),

$$SCR_{red}^{PLL} = SCR_{critical} - SCR_{critical}^{Q_{SC}=0} \tag{17}$$

From this critical SCR (SCR_{red}^{PLL}), the results are interpolated using both quadratic and linear fits as shown in Fig. 21. Results of the linear and quadratic fits are shown in the legend of Fig. 21. As with the FOS, the quadratic fit shows excellent accuracy, with a coefficient of determination of $R^2 = 0.99$ and a root mean square error (RMSE) of 0.01. The linear fit also performs well, achieving $R^2 = 0.95$ and RMSE $= 0.108$. Note that the simplified system model of Fig. 19 gives a value of $K_{PLL} = 1.01$, and from FOS, the value obtained was 1.05 (i.e. an error of less than 4%), validating this simplified system simulation model as a simple alternative to FOS to calculate K_{PLL} and other related issues. The complete similarity of Fig. 15 for FOS for a DFIG and Fig. 21 for the simplified simulation model with a generic IBR in Fig. 19, demonstrates the likely generality of the results for any RES that utilize a PLL control-loop.

These results suggest that K_Q is not significantly influenced by the SC model connected to the PCC. In particular, the subtransient impedance x_d'' of the SC does not have a significant impact on K_Q. Therefore, this value can be considered constant for a given IBR system, which has been found to be $K_Q = 2.05$ in the particular case of the typical parameter values used for the PLL in this paper. This value has been observed to depend primarily on the parameters related to the PLL. This relationship and the effect of the reactive power that the IBR may produce in the system is beyond the scope of this paper and will be explored in detail in a subsequent paper.

Fig. 22 shows the proposed equivalent circuit representing the Thévenin impedance seen from the IBR to easily calculate the impedance seen from the PLL control-loop, as in Fig. 13, but adding the effect of the SC reactive power contribution. As can be seen, by placing a parallel impedance of $1/(K_Q \cdot Q_{sc})$, the impedance seen by the PLL control-loop is modified.

As in Section IV-B for $Q_{SC} = 0$, Figs. 23 and 24 shows the real part of the eigenvalue λ_{PLL} in terms of the SCR when the SC injects $Q_{SC} = -0.5$ pu and $Q_{SC} = 0.5$ pu, respectively. The same procedure as described in Section IV-B is followed,

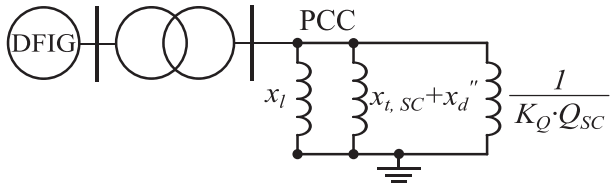

Fig. 22. Equivalent circuit representing the Thévenin impedance seen from the IBR model including a virtual impedance considering the SC reactive power operating point.

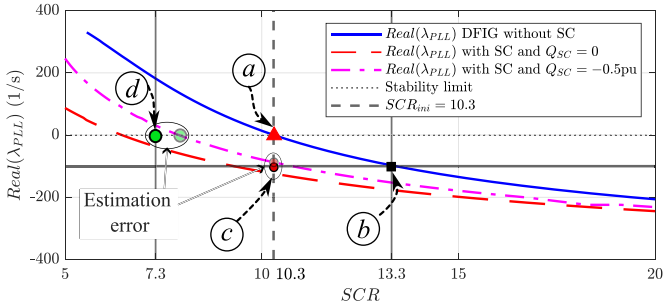

Fig. 23. Real part of the eigenvalue mostly related to the PLL-control-loop for the base case without SC and with SC producing $Q_{SC} = -0.5$ pu reactive power when the SCR is varied from 20 (50 km) to 5 (200 km).

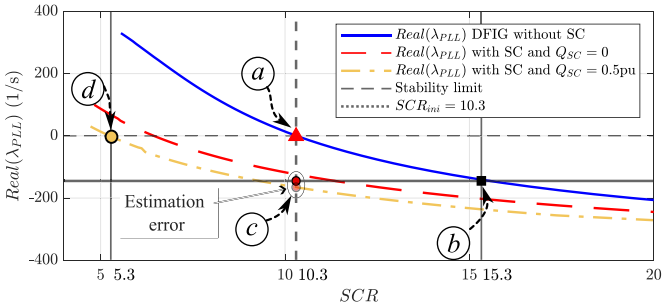

Fig. 24. Real part of the eigenvalue mostly related to the PLL control-loop for the base case without SC and with SC producing $Q_{SC} = 0.5$ pu reactive power when the SCR is varied from 20 (50 km) to 5 (200 km).

but now (14) is used to estimate the value of the SCR to obtain the new root-locus of the system when the SC is introduced. Note that points ⓐ, ⓑ, ⓒ and ⓓ have the same meaning as explained in Section IV-B. In this example, $SCR_{SC}^{st} = 2.98$ and therefore, $SCR = 13.3$ for $Q_{SC} = -0.5$ pu and $SCR_{SC}^{st} = 5.03$ and therefore, $SCR = 15.3$ for $Q_{SC} = 0.5$ pu. As shown in Table II, the error is 14% for $Q_{SC} = -0.5$ pu and 1% for $Q_{SC} = 0.5$ pu when estimating SCR_{SC}^{st} compared to using the full-order model simulations.

To clarify the steps involved in the estimation of the SCR in the presence of an SC providing or absorbing reactive power, a flowchart is presented in Fig. 9. The process begins by computing the initial SCR_{NETini} (point ⓐ in Figs. 10, 11, 23 and 24) of the DFIG without the SC, obtained from full-order simulations. Then, to determine the new SCR if an SC is installed in the system can be computed with two methods:

- Full-order simulations (FOS) incorporating all system dynamics
- Linear approximation proposed in this paper, based on (14).

TABLE II
SCR_{SC} VALUES WITH DIFFERENT MODELS AND Q_{SC}

Q_{SC} (pu_{SC})	SCR^0_{SC}	SCR^{Icc}_{SC}	$\boldsymbol{SCR^{st}_{SC}}$	SCR_{SC} FOS
−0.5	4.00 (53%)†	3.50 (34%)	2.98 (14%)	2.61
0.0	4.00 (1%)	4.00 (1%)	4.00 (1%)	3.95
0.5	4.00 (-19%)	4.50 (9%)	5.03 (1%)	4.96
1.0	4.00 (-30%)	5.00 (-12%)	6.05 (6%)	5.69

† The estimation error compared to the full-order simulation (FOS) is shown in parentheses next to each value.

If the FOS method is used, the SCR at which the system becomes unstable is obtained (SCR_{NET}, point ⓓ in Figs. 10, 11, 23 and 24). Then, to compute $SCR_{NETfinal}$, the difference between SCR_{NETini} and SCR_{NET} (SCR^{st}_{SC}) needs to be added to SCR_{NET}. If the proposed model in (14) is used, $SCR_{NETfinal}$ is obtained by considering the subtransient reactance of the SC, the impedance of the SC connection transformer, and an additional term proportional to Q_{SC}. Finally, $SCR_{NETfinal}$ is calculated by adding SCR^{st}_{SC} to the initial SCR_{NETini} of the DFIG prior to installing the SC. If no SC is added to the system, the total SCR remains equal to SCR_{NETini}, i.e., the SCR at which the IBR becomes unstable without the SC.

V. CONCLUSION

It has been confirmed that in a grid-following IBR, in which the PLL is essential, the PLL in the IBR is the main actor in the stability of the system. In addition, it has been shown that the root-locus of the IBR PLL depends mainly on the SCR value *seen* by the IBR. But also depends on the reactive power injected by the SC in a less, but not negligible, important way.

As the SCR at the PCC is a direct value of the admittance at the PCC, it has been shown that the main effect of the SC, and any other generation source that can be modeled from the small-signal point of view as a Thévenin, is to reduce the Thévenin impedance seen by the PLL at the PCC. In the case of the SC, the subtransient impedance, x''_d (plus the impedance of the connection transformer), is the SC impedance to consider both for short-circuit current estimation and for stability purposes. This idea is used to easily recalculate the PLL eigenvalues movement when an SC is connected.

When the SC reactive power, Q_{SC}, is not considered, the classical SCR, SCR^0_{SC}, accurately estimates both, the SC short-circuit current and the equivalent admittance at the PCC. However, when Q_{SC} is considered, the SC short-circuit current and the equivalent admittance at the PCC are affected differently. To accurately estimate the equivalent admittance at the PCC for stability purposes at different Q_{SC}, a new SCR linear function of the reactive power is proposed: $SCR^{st}_{SC} = SCR^0_{SC} + K_Q \cdot Q_{SC}$. A new Thévenin model has been proposed in accordance with this linear model. Results suggest that K_Q is not significantly influenced by the SC model connected to the PCC. In particular, the subtransient impedance x''_d of the SC does not have a significant impact on K_Q. Therefore, this value can be considered constant for a given IBR system, which has been found to be $K_Q \approxeq 2$ in the particular case of the typical parameter values used for the PLL in this paper. This value has been observed to depend primarily on the parameters related to the PLL.

While the proposed linear model is simple and effective, it does have some limitations. First, it has been developed and validated using a simplified system composed of a single DFIG and one synchronous compensator. This is useful for isolating key dynamic interactions, but it does not fully capture the complexity of realistic multi-infeed networks. Future work should validate and extend the proposed methodology to larger systems with multiple IBRs. Second, this study makes use of a linear approximation of a nonlinear (quadratic) relationship that closely fits the observed data. Future work could focus on the derivation of the coefficient K_{PLL} of the linear approximation, as a function of the known system parameters.

APPENDIX A
DOUBLY-FED INDUCTION GENERATOR MODEL

In this appendix, all the data related to the differential equations modeling the DFIG (taken from [30]) and the block diagrams of the control schemes used in this paper (taken from [31]) are provided.

A. DFIG Electromagnetic Equations

The stator and rotor voltage differential equations are defined by

$$\begin{aligned} v_{sd} &= R_s\, i_{sd} + \frac{1}{\omega_0}\frac{d\psi_{sd}}{dt} - \omega_s\, \psi_{sq} \\ v_{sq} &= R_s\, i_{sq} + \frac{1}{\omega_0}\frac{d\psi_{sq}}{dt} + \omega_s\, \psi_{sd} \\ v_{rd} &= R_r\, i_{rd} + \frac{1}{\omega_0}\frac{d\psi_{rd}}{dt} - (\omega_s - \omega_r)\, \psi_{rq} \\ v_{rq} &= R_r\, i_{rq} + \frac{1}{\omega_0}\frac{d\psi_{rq}}{dt} + (\omega_s - \omega_r)\, \psi_{rd} \end{aligned} \tag{18}$$

where v_{sd} and v_{sq} are the stator voltage components in the dq axes, v_{rd} and v_{rq} are the rotor voltage components; i_{sd}, i_{sq}, i_{rd}, and i_{rq} are the corresponding stator and rotor currents; ψ_{sd}, ψ_{sq}, ψ_{rd}, and ψ_{rq} represent the stator and rotor magnetic flux linkages; R_s and R_r are the stator and rotor resistances; ω_0 is the base angular frequency; ω_s is the synchronous speed; and ω_r is the rotor speed.

The flux-current relations are given by

$$\begin{aligned} \psi_{sd} &= L_s\, i_{sd} + L_m\, i_{rd} \\ \psi_{sq} &= L_s\, i_{sq} + L_m\, i_{rq} \\ \psi_{rd} &= L_r\, i_{rd} + L_m\, i_{sd} \\ \psi_{rq} &= L_r\, i_{rq} + L_m\, i_{sq} \end{aligned} \tag{19}$$

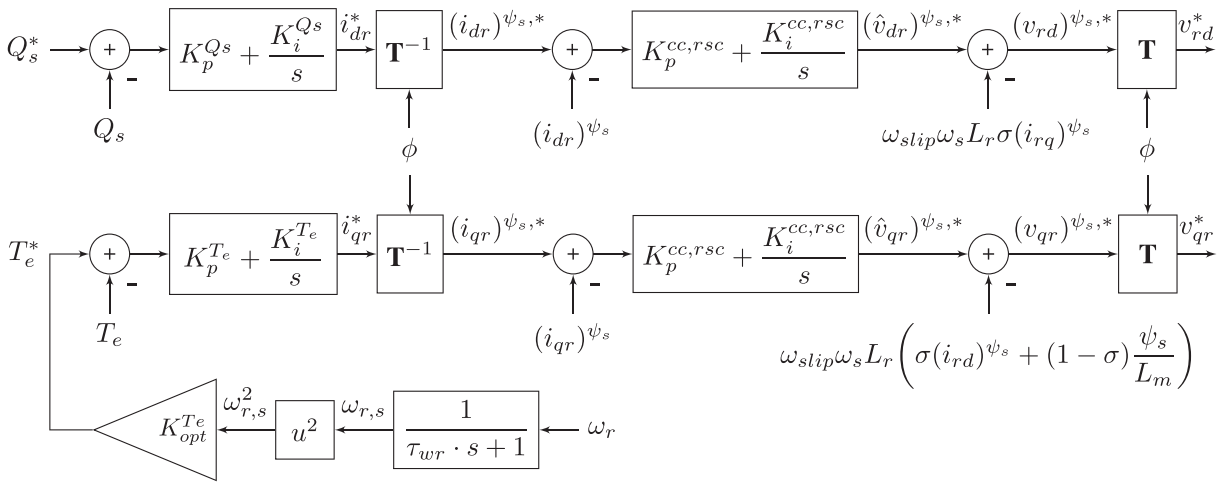

Fig. 25. Rotor side converter controllers block diagrams.

where L_s and L_r are the self-inductances of the stator and rotor, respectively, and L_m is the mutual inductance.

The stator and rotor inductances are expressed as

$$L_s = L_{\sigma s} + L_m$$
$$L_r = L_{\sigma r} + L_m \tag{20}$$

with $L_{\sigma s}$ and $L_{\sigma r}$ being the leakage inductances of the stator and rotor.

The equations of the GSC output filter are given by

$$v_{ad} = -R_a\, i_{ad} - \frac{1}{\omega_0}\frac{d\psi_{ad}}{dt} + \omega_s\, \psi_{aq} - v_{sd}$$
$$v_{aq} = -R_a\, i_{aq} - \frac{1}{\omega_0}\frac{d\psi_{aq}}{dt} - \omega_s\, \psi_{ad} \tag{21}$$

where v_{ad} and v_{aq} are the filter voltage components in the dq axes; i_{ad} and i_{aq} are the filter currents; ψ_{ad} and ψ_{aq} are the flux linkages in the filter inductor; and R_a is the filter resistance.

Finally, the inductor flux is defined by

$$\psi_{ad} = L_a\, i_{ad}$$
$$\psi_{aq} = L_a\, i_{aq} \tag{22}$$

where L_a is the filter inductance.

B. DFIG Electromechanical Equations

The rotor swing equation is defined by

$$2H\omega_s \frac{\mathrm{d}\omega_{slip}}{\mathrm{d}t} = T_m - T_e \tag{23}$$

being T_m and T_e the mechanical torque applied to the shaft and the electrical torque extracted from the shaft, calculated as

$$T_e = \psi_{qr} i_{dr} - \psi_{dr} i_{qr} \tag{24}$$

and being the slip frequency ω_{slip}

$$\omega_{slip} = \frac{\omega_s - \omega_r}{\omega_s} \tag{25}$$

TABLE III
DOUBLY FED INDUCTION GENERATOR PARAMETERS

Parameter	Description	Value [pu]
R_s	stator resistance	0.00734
$L_{\sigma s}$	stator leakage inductance	0.1178
R_r	rotor resistance	0.01225
$L_{\sigma r}$	rotor leakage inductance	0.15349
L_m	magnetizing inductance	4.709
r_a	output filter resistance	0.1
L_a	output filter inductance	1
c	DC-link capacitance	0.0555
h	inertia	3.3 [s]
L_t	transformer inductance	0.15
r_t	transformer resistance	0.015
c_f	output filter capacitance	0.11
BW_{cc}	current controllers bandwidth	1500 [rad/s]
BW_{PLL}	PLL bandwidth	35% BW_{cc}
K_{opt}^{Te}	optimal torque gain	0.5896
BW_v	voltage control bandwidth	10% BW_{cc}
ζ	controllers damping	$1/\sqrt{2}$

C. DFIG Rotor and Grid Side Converter Controllers

The DFIG controllers are taken from [31]. The rotor-side converter (RSC) and grid-side converter (GSC) controllers are shown in Figs. 25 and 26, respectively. It should be noted that a reference frame solid to the stator-flux is considered. Therefore, in order to transform the rotor currents and voltages dq-axis to the stator-flux reference frame:

$$\begin{bmatrix} x_{rd} \\ x_{rq} \end{bmatrix} = \underbrace{\begin{bmatrix} \cos\phi & -\sin\phi \\ \sin\phi & \cos\phi \end{bmatrix}}_{\mathbf{T}} \begin{bmatrix} x_{rd} \\ x_{rq} \end{bmatrix}^{\psi_x} \tag{26}$$

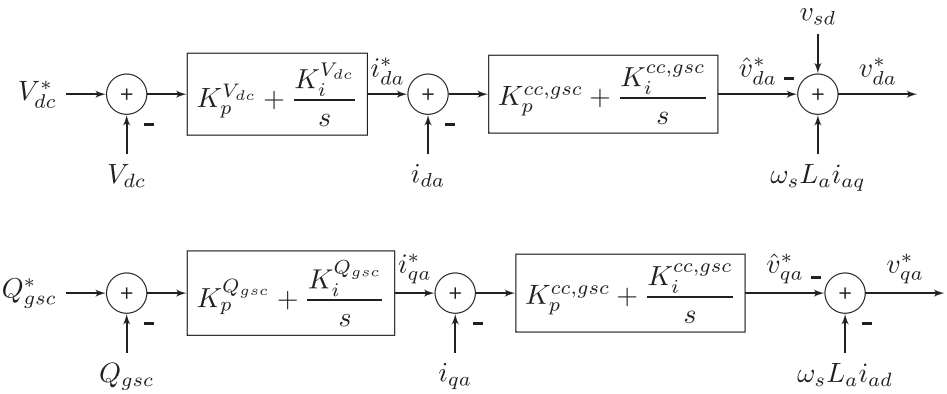

Fig. 26. Grid side converter controllers block diagrams.

being ϕ calculated as

$$\phi = \arctan \frac{\psi_{sd}}{\psi_{sq}} \tag{27}$$

and the stator-flux module $\psi_s = \sqrt{\psi_{sd}^2 + \psi_{sq}^2}$ and

$$\sigma = L_r - \frac{L_m^2}{L_s} \tag{28}$$

APPENDIX B
SYNCHRONOUS COMPENSATOR MODEL

In this section, all the data related to the differential equations and automatic voltage regulator (AVR) of the synchronous compensator are provided [13].

A. SC Electromagnetic Equations

The per unit stator voltage equations are defined as

$$\begin{aligned} e_d &= \frac{1}{\omega_0}\frac{d\psi_d}{dt} - \psi_q\,\omega_r - R_a\,i_d \\ e_q &= \frac{1}{\omega_0}\frac{d\psi_q}{dt} + \psi_d\,\omega_r - R_a\,i_q \end{aligned} \tag{29}$$

where e_d and e_q are the stator voltage components in the d and q axes, respectively; ψ_d and ψ_q are the stator flux linkages; i_d and i_q are the stator currents; ω_0 is the base angular frequency; ω_r is the rotor (electrical) speed; and R_a is the stator resistance.

The per unit rotor voltage equations are given by

$$\begin{aligned} e_{fd} &= \frac{1}{\omega_0}\frac{d\psi_{fd}}{dt} + R_{fd}\,i_{fd} \\ 0 &= \frac{1}{\omega_0}\frac{d\psi_{1d}}{dt} + R_{1d}\,i_{1d} \\ 0 &= \frac{1}{\omega_0}\frac{d\psi_{1q}}{dt} + R_{1q}\,i_{1q} \\ 0 &= \frac{1}{\omega_0}\frac{d\psi_{2q}}{dt} + R_{2q}\,i_{2q} \end{aligned} \tag{30}$$

where e_{fd} is the rotor field voltage, ψ_{fd} is the rotor field flux linkage, and i_{fd} is the rotor field current; R_{fd} is the rotor field resistance; ψ_{1d}, ψ_{1q}, and ψ_{2q} are the flux linkages associated with the damping rotor windings, with i_{1d}, i_{1q}, and i_{2q} being the corresponding damping rotor currents; and R_{1d}, R_{1q}, and R_{2q} are the resistances of these windings.

The stator and rotor per unit flux linkage equations are defined as

$$\begin{aligned} \psi_d &= -\left(L_{ad} + L_l\right) i_d + L_{ad}\,i_{fd} + L_{ad}\,i_{1d} \\ \psi_q &= -\left(L_{aq} + L_l\right) i_q + L_{aq}\,i_{1q} + L_{aq}\,i_{2q} \\ \psi_{fd} &= L_{ffd}\,i_{fd} + L_{fld}\,i_{1d} - L_{ad}\,i_d \\ \psi_{1d} &= L_{fld}\,i_{fd} + L_{11d}\,i_{1d} - L_{ad}\,i_d \\ \psi_{1q} &= L_{11q}\,i_{1q} + L_{aq}\,i_{2q} - L_{aq}\,i_q \\ \psi_{2q} &= L_{aq}\,i_{1q} + L_{22q}\,i_{2q} - L_{aq}\,i_q \end{aligned} \tag{31}$$

where L_{ad} and L_{aq} are the stator mutual inductances in the d and q axes, respectively; L_l is the stator leakage inductance; L_{ffd} is the rotor field winding self-inductance, and L_{fld} is the mutual inductance between the rotor field winding and the first d-axis damping winding; L_{11d} and L_{11q} are the self-inductances associated with the first damping rotor winding, and L_{22q} is the self-inductance associated with the second damping rotor winding.

Finally, a simplifying transformation is applied to the inductance expressions:

$$\begin{aligned} L_{fd} &= L_{ffd} - L_{fld} \\ L_{1d} &= L_{11d} - L_{fld} \\ L_{1q} &= L_{11q} - L_{aq} \\ L_{2q} &= L_{22q} - L_{aq} \end{aligned} \tag{32}$$

where L_{fd}, L_{1d}, L_{1q}, and L_{2q} are the simplified excitation and damping rotor inductances. The relation between the electromagnetic parameters to the classical parameters definition can be expressed as below. For the d-axis windings,

$$L_{fd} = L_{ad} \cdot \frac{L'_d - L_{\sigma l}}{L_d - L'_d},\ r_{fd} = \frac{L_{ad} + L_{fd}}{T'_{d0} \cdot \omega_0},$$

$$L_{kd} = \frac{(L'_d - L_{\sigma l}) \cdot (L''_d - L_{\sigma l})}{L'_d - L''_d},$$

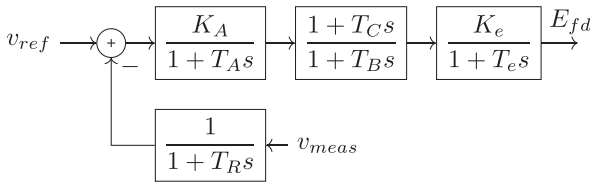

Fig. 27. Automatic voltage regulator used.

$$r_{kd} = \frac{L_{kd} + L'_d - L_{\sigma l}}{T''_{d0} \cdot \omega_0},$$
$$T'_d = T'_{d0} \cdot \frac{L'_d}{L_d}. \tag{33}$$

and for the q-axis windings,

$$L_{kq1} = L_{aq} \cdot \frac{L'_q - L_{\sigma l}}{L_q - L'_q},\ r_{kq1} = \frac{L_{aq} + L_{kq1}}{T'_{q0} \cdot \omega_0},$$
$$L_{kq2} = \frac{(L'_q - L_{\sigma l}) \cdot (L''_q - L_{\sigma l})}{L'_q - L''_q},$$
$$r_{kq2} = \frac{L_{kq2} + L'_q - L_{\sigma l}}{T''_{q0} \cdot \omega_0},$$
$$T''_q = T''_{q0} \cdot \frac{L''_q}{L'_q}. \tag{34}$$

with

$$L_d = L_{ad} + L_{\sigma l},$$
$$L_q = L_{aq} + L_{\sigma l} \tag{35}$$

It should be noted that, as the stator frequency is equal to the base frequency, the per unit reactance (x) and the per unit inductance (L) are equal, i.e. the inductances relate directly to the reactances in Table IV.

B. Synchronous Compensator Electromechanical Equations

The rotor swing equation in per-unit for a synchronous machine is given by:

$$2H \frac{\mathrm{d}\omega_r}{\mathrm{d}t} = T_m - T_e \tag{36}$$

where T_m and T_e represent the mechanical torque applied to the shaft and the electrical torque extracted from the shaft, respectively. The electrical torque is calculated as:

$$T_e = \psi_q i_d - \psi_d i_q \tag{37}$$

where ψ_d and ψ_q are the flux linkages in the direct and quadrature axes, respectively, and i_d and i_q are the corresponding stator currents.

C. SC Automatic Voltage Regulator Model

In this work, it has been adopted the automatic voltage regulator (AVR) shown in Fig. 27. The differential equations used to model the electromagnetic and electromechanical dynamics for the synchronous machine are taken from [13].

TABLE IV
SYNCHRONOUS COMPENSATOR PARAMETERS

Parameter	Description	Value [pu]
R_s	stator resistance	0.018
H	inertia including flywheel	8.2
D	friction coefficient	0.01
$x_{\sigma l}$	stator leakage inductance	0.1
$r_{\sigma fd}$	excitation winding leakage resistance	$5.2 \cdot 10^{-4}$
x_d	unsaturated d-axis stator inductance	1.6
x_d^s	saturated d-axis stator inductance	1.5
x_q	unsaturated q-axis stator inductance	0.66
x_q^S	saturated q-axis stator inductance	0.62
$x_d^{'}$	unsaturated d-axis stator transient inductance	0.23
$x_d^{'s}$	saturated d-axis stator subtran. inductance	0.20
$x_d^{''}$	unsaturated d-axis stator transient inductance	0.15
$x_d^{''s}$	saturated d-axis stator subtran. inductance	0.13
$x_q^{''}$	unsaturated q-axis stator subtran. inductance	0.22
$x_q^{''s}$	saturated q-axis stator subtran. inductance	0.2
T'_d	d-axis transient time constant	1.3
T''_d	d-axis subtransient time constant	0.03
T'_{d0}	d-axis open circuit transient time constant	10
T'_q	q-axis transient time constant	1.1
T''_q	q-axis subtransient time constant	0.15
T'_{q0}	q-axis open circuit transient time constant	15
T''_{d0}	d-axis open circuit subtransient time constant	0.04
K_A	main voltage regulator gain	200
T_A	main voltage regulator delay	10 [ms]
T_C	washout filter numerator	1
T_B	washout filter denominator	12
K_E	diode bridge gain	1
T_E	diode bridge delay	1.15 [s]
T_R	measure filter delay	10 [ms]

REFERENCES

[1] P. Tielens and D. Van Hertem, "The relevance of inertia in power systems," *Renewable Sustain. Energy Rev.*, vol. 55, pp. 999–1009, Mar. 2016.
[2] A. Tayyebi, D. Groß, A. Anta, F. Kupzog, and F. Dörfler, "Frequency stability of synchronous machines and grid-forming power converters," *IEEE Trans. Emerg. Sel. Topics Power Electron.*, vol. 8, no. 2, pp. 1004–1018, Jun. 2020.
[3] E. Marrazi, G. Yang, and P. Weinreich-Jensen, "Allocation of synchronous condensers for restoration of system short-circuit power," *J. Modern Power Syst. Clean Energy*, vol. 6, no. 1, pp. 17–26, Jan. 2018.
[4] L. Richard, Nahid-Al-Masood, T. K. Saha, W. Tushar, and H. Gu, "Optimal allocation of synchronous condensers in wind dominated power grids," *IEEE Access*, vol. 8, pp. 45400–45410, 2020.
[5] D. B. Rathnayake et al., "Grid forming inverter modeling, control, and applications," *IEEE Access*, vol. 9, pp. 114781–114807, 2021.
[6] S. Hadavi, S. P. Me, B. Bahrani, M. Fard, and A. Zadeh, "Virtual synchronous generator versus synchronous condensers: An electromagnetic transient simulation-based comparison," in *Proc. CIGRE Sci. Eng.*, Feb. 2023, pp. 10–16.

[7] L. Ding, X. Lu, and J. Tan, "Small-signal stability analysis of low-inertia power grids with inverter-based resources and synchronous condensers," in *Proc. IEEE Power Energy Soc. Innov. Smart Grid Technol. Conf.*, New Orleans, LA, USA: IEEE, Apr. 2022, pp. 1–5.
[8] J. Jia, G. Yang, A. H. Nielsen, E. Muljadi, P. Weinreich-Jensen, and V. Gevorgian, "Synchronous condenser allocation for improving system short circuit ratio," in *Proc. 5th Int. Conf. Electric Power Energy Convers. Syst.*, Apr. 2018, pp. 1–5.
[9] M. Caldora et al., "Synchronous condensers with flywheel for power systems with high penetration of RES: The case of italian transmission grid," in *Proc. 2022 AEIT Int. Annu. Conf.*, Oct. 2022, pp. 1–5.
[10] J. Geis-Schroer, A. R. Nair, S. Patel, and S. Kamalasadan, "Modeling and analysis of weak grid considering phase locked loop and synchronous condenser effect on grid stability," in *Proc. IEEE Int. Conf. Power Electron. Smart Grid Renewable Energy*, Jan. 2020, pp. 1–6.
[11] F. O. Igbinovia, G. Fandi, Z. Muller, J. Svec, and J. Tlusty, "Optimal location of the synchronous condenser in electric-power system networks," in *Proc. 17th Int. Sci. Conf. Electric Power Eng.*, Prague, Czech Republic: IEEE, May 2016, pp. 1–6.
[12] W. Tian, J. Gong, Y. Li, P. Chen, H. Wei, and W. Xu, "Optimal configuration of distributed synchronous condenser for high-proportion renewable sending end power grid," in *Proc. IEEE 5th Int. Elect. Energy Conf.*, Nangjing, China: IEEE, May 2022, pp. 3759–3764.
[13] P. Kundur, N. Balu, and M. Lauby, *Power System Stability and Control, Ser. EPRI Power System Engineering Series*. New York, NY, USA: McGraw-Hill Education, 1994.
[14] North American Electric Reliability Corporation (NERC), "Integrating inverter-based resources into low short circuit strength systems, reliability guideline," Dec. 2017. Accessed: Jan. 27, 2023. [Online]. Available: https://www.nerc.com/comm/RSTC_Reliability_Guidelines/Item_4a._Integrating%20_Inverter-Based_Resources_into_Low_Short_Circuit_Strength_Systems_-_2017-11-08-FINAL.pdf
[15] Australian Energy Market Operator (AEMO), "System strength in the NEM explained," Mar. 2020. Accessed: Jan. 27, 2023. [Online]. Available: https://aemo.com.au/-/media/files/electricity/nem/system-strength-explained.pdf?la=en
[16] Red Eléctrica de España (REE), "Criterios técnicos de evaluación de fortaleza de red para integración de MPE de acuerdo a la literatura técnica existente," 2021. Accessed: Jan. 27, 2023. [Online]. Available: https://www.ree.es/sites/default/files/12_CLIENTES/Documentos/Entregable1_Criterios_t%C3%A9cnicos_integraci%C3%B3n_MPE.pdf
[17] P. Noorcheshma, J. Sreedevi, and V. Sivaprasad, "Low voltage ride through (LVRT) of DFIG and PMSM wind turbine," in *Proc. IEEE Int. Conf. Elect., Comput. Commun. Technol.*, Mar. 2015, pp. 1–5.
[18] *IEEE Guide for Planning DC Links Terminating at AC Locations Having Low Short-Circuit Capacities*, IEEE Standard 1204-1997, pp. 1–216, Jan. 1997.
[19] O. Damanik, O. C. Sakinci, G. Grdenic, and J. Beerten, "Evaluation of the use of short-circuit ratio as a system strength indicator in converter-dominated power systems," in *Proc. IEEE PES Innov. Smart Grid Technol. Conf. Europe (ISGT-Europe)*, Novi Sad, Serbia: IEEE, Oct. 2022, pp. 1–5.
[20] M. O. Qays, I. Ahmad, D. Habibi, A. Aziz, and T. Mahmoud, "System strength shortfall challenges for renewable energy-based power systems: A review," *Renewable Sustain. Energy Rev.*, vol. 183, Sep. 2023, Art. no. 113447.
[21] J. S. Bryant, B. McGrath, L. Meegahapola, and P. Sokolowski, "Small-signal stability analysis of voltage source inverters operating under low short-circuit ratios," in *Proc. IEEE Madrid PowerTech*, Jun. 2021, pp. 1–6.
[22] Y. Zhang, S.-H. F. Huang, J. Schmall, J. Conto, J. Billo, and E. Rehman, "Evaluating system strength for large-scale wind plant integration," in *Proc. IEEE PES Gen. Meeting Conf. Expo.*, Jul. 2014, pp. 1–5.
[23] Minnesota Department of Commerce, "Minnesota renewable energy integration and transmission study (MRITS)," 2014. Accessed: Jan. 27, 2023. [Online]. Available: https://mn.gov/commerce-stat/pdfs/mrits-report-2014.pdf
[24] D. Wu, G. Li, M. Javadi, A. M. Malyscheff, M. Hong, and J. N. Jiang, "Assessing impact of renewable energy integration on system strength using site-dependent short circuit ratio," *IEEE Trans. Sustain. Energy*, vol. 9, no. 3, pp. 1072–1080, Jul. 2018.
[25] C. Liu, H. Xin, D. Wu, H. Gao, H. Yuan, and Y. Zhou, "Generalized operational short-circuit ratio for grid strength assessment in power systems with high renewable penetration," *IEEE Trans. Power Syst.*, vol. 39, no. 4, pp. 5479–5494, Jul. 2024.
[26] W. Dong, H. Xin, D. Wu, and L. Huang, "Small signal stability analysis of multi-infeed power electronic systems based on grid strength assessment," *IEEE Trans. Power Syst.*, vol. 34, no. 2, pp. 1393–1403, Mar. 2019.
[27] G. Wang, Y. Huang, and Z. Xu, "Voltage stiffness for strength evaluation of VSC-penetrated power systems," *IEEE Trans. Power Syst.*, vol. 39, no. 4, pp. 6119–6122, Jul. 2024.
[28] C. Henderson, A. Egea-Alvarez, T. Kneuppel, G. Yang, and L. Xu, "Grid strength impedance metric: An alternative to SCR for evaluating system strength in converter dominated systems," *IEEE Trans. Power Del.*, vol. 39, no. 1, pp. 386–396, Feb. 2024.
[29] W. Rui, S. Qiuye, M. Dazhong, and H. Xuguang, "Line impedance cooperative stability region identification method for grid-tied inverters under weak grids," *IEEE Trans. Smart Grid*, vol. 11, no. 4, pp. 2856–2866, Jul. 2020.
[30] L. Rouco and J. L. Zamora, "Dynamic patterns and model order reduction in small-signal models of doubly fed induction generators for wind power applications," in *Proc. IEEE Power Eng. Soc. Gen. Meeting*, Montreal, QC, Canada: IEEE, 2006, pp. 1–8.
[31] F. Mei and B. C. Pal, "Modelling of doubly-fed induction generator for power system stability study," in *Proc. IEEE Power Energy Soc. Gen. Meeting - Convers. Del. Elect. Energy 21st Century*, Pittsburgh, PA, USA: IEEE, Jul. 2008, pp. 1–8.
[32] J. Hu, Y. Lei, Y. Chi, and X. Tian, "Analysis on the inertia and the damping characteristics of DFIG under multiple working conditions based on the grid-forming control," *Energy Reports*, vol. 8, pp. 591–604, Nov. 2022.
[33] G. Abad, J. Lopez, M. Rodriguez, L. Marroyo, and G. Iwanski, *Doubly Fed Induction Machine: Modeling and Control for Wind Energy Generation*. Hoboken, NJ, USA: Wiley, 2011.
[34] C. Guo, C. Zhao, R. Iravani, H. Ding, and X. Wang, "Impact of phase-locked loop on small-signal dynamics of the line commutated converter-based high-voltage direct-current station," *IET Gener., Transmiss. Distribution*, vol. 11, no. 5, pp. 1311–1318, 2017.
[35] J. Z. Zhou, H. Ding, S. Fan, Y. Zhang, and A. M. Gole, "Impact of short-circuit ratio and phase-locked-loop parameters on the small-signal behavior of a VSC-HVDC converter," *IEEE Trans. Power Del.*, vol. 29, no. 5, pp. 2287–2296, Oct. 2014.
[36] T. Gu, P. Wang, D. Liu, A. Sun, D. Yang, and G. Yan, "Modeling and small-signal stability analysis of doubly-fed induction generator integrated system," *Glob. Energy Interconnection*, vol. 6, no. 4, pp. 438–449, Aug. 2023.
[37] I. J. Perez-arriaga, G. C. Verghese, and F. C. Schweppe, "Selective modal analysis with applications to electric power systems, PART I: Heuristic introduction," *IEEE Trans. Power App. Syst.*, vol. PAS-101, no. 9, pp. 3117–3125, Sep. 1982.
[38] K. W. Klontz, T. J. E. Miller, M. I. McGilp, H. Karmaker, and P. Zhong, "Short-circuit analysis of permanent-magnet generators," *IEEE Trans. Ind. Appl.*, vol. 47, no. 4, pp. 1670–1680, Jul./Aug. 2011.

Jorge Suárez-Porras (Student Member, IEEE) received the M.Sc. degree in energy engineering - power electronics and drives from Aalborg University, Aalborg, Denmark, in 2022. He is currently working toward the Ph.D. degree with the Institute for Research in Technology, Universidad Pontificia Comillas, Madrid, Spain. He is a Research Assistant with the Institute for Research in Technology, Universidad Pontificia Comillas. The Ph.D. thesis topic is on the use of synchronous compensators to facilitate the penetration of renewable energy sources.

Fidel Fernández-Bernal received the B.S., M.S., and Ph.D. degrees in electrical engineering from the Universidad Pontificia Comillas de Madrid, Madrid, Spain, in 1990, 1994, and 2000, respectively. He was the Head of the Electrical Department from 2010 to 2019, where he is currently a Full Professor and the Head of the Electric Machines and Drives Lab. He develops his research with the Institute for Research in Technology, Universidad Pontificia Comillas, Madrid.

Luis Rouco (Senior Member, IEEE) received the Ingeniero Industrial and Doctor Ingeniero Industrial degrees from the Universidad Politécnica de Madrid, Madrid, Spain, in 1985 and 1990, respectively. He was the Head of the Department of Electrical Engineering from 1999 to 2005. He was a Visiting Scientist with Ontario Hydro, MIT, and ABB Power Systems. He is currently a Full Professor with Universidad Pontificia Comillas, Madrid. He develops his research activities with the Instituto de Investigación Tecnológica, Madrid. Prof. Rouco is a Distinguished Member of Cigré and the Member of the Executive Committee of Spanish National Committee of Cigré.

Andrés Tomás-Martín received the M.Sc. degree in energy from Universidad Complutense de Madrid, Madrid, Spain, in 2019. He is currently working toward the Ph.D. degree with the Institute for Research in Technology, Universidad Pontificia Comillas, Madrid. He is currently a Research Assistant with the Institute for Research in Technology, Universidad Pontificia Comillas. His research interests include decentralised control of microgrids and small-signal analysis of power systems.